Understanding the electrochemical reaction mechanism to achieve excellent performance of the conversion-alloying Zn_2SnO_4 anode for Li-ion batteries

Maciej Moździerz[1], Zhenhe Feng[2,#], Agnieszka Brzoza-Kos[1], Paweł Czaja[3], Boyang Fu[1], Konrad Świerczek[1,4,*]

[1]AGH University of Science and Technology, Faculty of Energy and Fuels,
al. Mickiewicza 30, 30-059 Krakow, Poland
[2]State Key Laboratory of Space Power-Sources Technology, Shanghai Institute of Space Power-Sources, no. 2965 Dongchuan Road, Shanghai 200245, China
[3]Institute of Metallurgy and Materials Science, Polish Academy of Sciences, 25 ul. Reymonta, 30-059 Krakow, Poland
[4]AGH Centre of Energy, AGH University of Science and Technology,
ul. Czarnowiejska 36, 30-054 Krakow, Poland
[#]zhenhefeng2021@163.com
[*]xi@agh.edu.pl

Supplementary Information

Table S1. Comparison of the recently reported electrochemical performance of bare and modified M_2SnO_4 (M = Zn, Co, Mn) electrodes.

No	Materials	Synthesis method	Initial dis-/charge (mAh/g)	Current density (mA/g)	Rate capability (mAh/g) /current density (mA/g)	Stability (mAh/g) /current density /number of cycles	Composition of electrode (active material: conductive material: binder)	Binder /electrolyte type	Ref.
1	Zn_2SnO_4	hydro-thermal	1344 /543	60	24 /2400	186 /60 /100	70:20:10	PVDF /1M $LiPF_6$@ EC/DMC (1:1,v:v)	[1]
2	Zn_2SnO_4	hydro-thermal	- /614	50	91 /1000	-	70:20:10	PVDF /1M $LiPF_6$@ EC/DMC (1:1,v:v)	[2]
	Zn_2SnO_4 /graphene		- /1052	50	672 /1000	848 /1000 /200			
3	Zn_2SnO_4 (nanoparticles)	hydrothermal	1024 /482	100	68 /1000	147 /100 /100	70:20:10	PVDF/ 1M $LiPF_6$@ EC/EMC /DMC(1:1:1,v:v:v)	[3]

4	Zn_2SnO_4 (microspheres)	spray pyrolysis	1580 /1011	-	302 /5000	81 /1000 /120	70:20:10	CMC/ 1M $LiPF_6$@ FEC/DMC(1:1,v:v)	[4]
5	Zn_2SnO_4	hydrothermal	1217 /625	100	93.2 /1000	272 /100 /30	70:20:10	PVDF/ 1M $LiPF_6$@ EC/DMC (1:1,v:v)	[5]
	Zn_2SnO_4/ CNT		1925 /1065		252 /1000	686 /100 /30			
6	Zn_2SnO_4 (nanoparticles)	hydrothermal	1030 /467	200	34 /650	234 /700 /50	80:10:10	PVDF/ 1.3M $LiPF_6$@ EC/EMC (3/7)+15 wt%FEC	[6]
7	Zn_2SnO_4 (nanorods)	hydrothermal	1100/-	100	/	51 /1000 /100	70:15:15	PVDF/ 1M $LiPF_6$@ EC/PC/ DEC(3:1:1,v:v:v)	[7]
8	Zn_2SnO_4	hydrothermal	1216 /812	200	/	498 /200 /20	70:15:15	PVDF/ 1M $LiPF_6$@ EC/DEC (1:1,v:v)	[8]
9	Zn_2SnO_4 (hollow boxes)	co-precipitation and alkali etching	1555 /884	300	300 /2400	540 /300 /45	65:15:20	PVDF/ 1M $LiPF_6$@ EC/DMC /DEC(1:1:1,v:v:v)	[9]
10	Zn_2SnO_4 (hollow nano-spheres)	hydrothermal	1618 /1071	100	471 /1000	443 /1000 /60	75:15:10	CMC/ 1M $LiPF_6$@ EC/DMC /DEC(1:1:1,v:v:v)	[10]
11	Zn_2SnO_4	hydrothermal	1630 /929	50	306 /200	544 /100 /20	80:10:10	PVDF/ 1M $LiPF_6$@ EC/EMC /DMC(1:1:1,v:v:v)	[11]
12	Zn_2SnO_4	hydrothermal	1714 /836	50	412 /1600	406 /50 /50	75:15:10	PVDF/ 1M $LiPF_6$@ EC/DMC (1:1,v:v)	[12]

13	Zn_2SnO_4 (nanowires)	vapor transport	1650 /1000	120	/	695 /120 /60	70:15:15	PVDF/ 1M $LiPF_6$@ EC/DMC (1:1,v:v)	[13]
14	Zn_2SnO_4 (cubes)	hydrothermal	1437 /921	50	/	775 /50 /20	40:40:20	PVDF/ No description	[14]
15	Zn_2SnO_4	hydrothermal	1324 /359	500	/	110 /500 /20	70:20:10	PVDF/ 1M $LiPF_6$@ EC/DMC /EMC(1:1:1,v:v:v)	[15]
16	Zn_2SnO_4	hydrothermal	1521 /1007	50	412 /400	100 /200 /50	75:15:10	PVDF/ 1M $LiPF_6$@ EC/DMC (1:1,v:v)	[16]
17	Zn_2SnO_4	hydrothermal	1671 /690	100	/	343 /100 /40	70:15:15	PVDF/ 1M $LiPF_6$@ EC/DMC /EMC(1:1:1,v:v:v)	[17]
18	Zn_2SnO_4	mechano chemical	1247 /666	/	/	150 / - /30	80:10:10	PVDF/ 1M $LiPF_6$@ EC/DMC (1:1,v:v)	[18]
19	Zn_2SnO_4	solid-state reaction	2054 /1025	50	/	689 /50 /50	40:40:20	PVDF/ 1M $LiPF_6$@ EC/DEC (1:1,v:v)	[19]
20	Zn_2SnO_4	hydrothermal	1634 /710	60	/	405 /60 /40	70:15:15	PVDF/ 1M $LiPF_6$@ EC/DMC /EMC(1:1:1,v:v:v)	[20]
21	Zn_2SnO_4	supercritical water hydrothermal	1526 /1093	50	/	856 /50 /50	85:5:10	PVDF/ 1M $LiPF_6$@ EC/DEC (1:1,v:v)	[21]
22	Zn_2SnO_4	hydrothermal	1904 /1046	50	/	625 / - /20	40:40:20	PTFE/ 1M $LiClO_4$@ EC/DMC (1:1,v:v)	[22]

23	Zn_2SnO_4 (cubic shape)	hydrothermal	1389 /914	100	/	580 /100 /50	80:15:5	PTFE/ 1M $LiPF_6$@ EC/PC/DMC(6:3:1,v:v:v)	[23]
24	Zn_2SnO_4	no description	1360 /857	200	142 /2000	162 /200 /95	70:20:10	CMC/ 1M $LiPF_6$@ EC/DMC (1:1,v:v)	[24]
25	Zn_2SnO_4/ RGO	hydrothermal	2081 /969	55	591 /2735	983 /55 /100	60:20:20	PAA/ 1M $LiPF_6$@ EC/EMC /DMC(1:1:1,v:v:v) +5wt% FEC	[25]
26	Co_2SnO_4	hydrothermal	1442 /1052	100	151 /1000	195 /100 /100	50:30:20	LA132/ 1M $LiPF_6$@ EC/DEC/ EMC(1:1:1,v:v:v)	[26]
27	Mg_2SnO_4 (nanoparticles)	co-precipitation	928 /507	0.2 mA/ cm^2	/	392 /0.2 mA/cm^2 /100	80:12:8	PTFE/ 1M $LiClO_4$@ EC/DMC (1:1,v:v)	[27]
28	Mn_2SnO_4 (nanoparticles)	hydrothermal microemulsion	1320 /552	0.07 mA/ cm^2	/	143 /0.07 mA/cm^2 /100	70:20:10	PVDF/ 1M $LiPF_6$@ EC/DEC(1:1,v:v)	[28]
29	**Zn_2SnO_4**	**solid-state route**	**1326 /864** **1279 /756**	**50** **200**	**461 /1000**	**631 /200 /100** **533 /500 /100**	**70:20:10**	**CMC+ SBR/ 1M $LiPF_6$@ EC/DEC (1:1,v:v) +5wt% FEC+ 1wt% VC**	**our work**

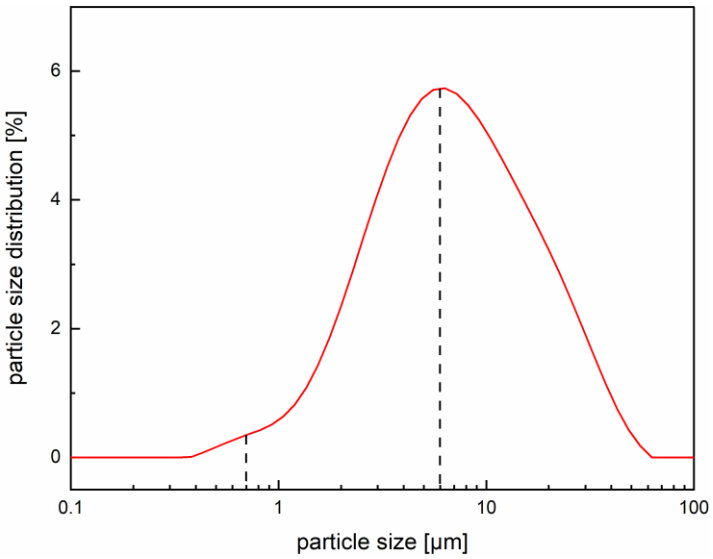

Figure S1. Particle size distribution for the Zn_2SnO_4 powder used to prepare electrodes, measured using DLS method. The distribution shows two maxima: the less intense at ca. 0.7 µm, and the more intense at ca. 6 µm. Sizes above 10 µm likely correspond to the agglomerated primary particles.

Supplementary Note 1: Charge transfer during (de-)lithiation studied by EIS measurements and DRT analysis

To get an insight into the influence of different lithiation levels on charge transfer EIS measurements were conducted. The voltage profile for the Zn_2SnO_4-based half-cell is presented in Figure S2a. The spectra were collected at the marked points. All the measured EIS data are presented collectively in Figures S2b-d. To analyze the data, the distribution of relaxation times (DRT) approach was used, as described in the Experimental section. It allows resolving various processes from the total impedance, especially the ones characterized by similar time constants, which otherwise would be hard to analyze unambiguously using the conventional equivalent circuit fitting. The area under each observed peak corresponds to the resistance related to a given polarization effect. The results of DRT calculations are presented in Figure S2e-g, for the 1st lithiation, 1st delithiation, and 2nd lithiation, respectively. The data are analyzed in the 1-10^6 Hz frequency range, to exclude the Warburg diffusion part, as the DRT method can be used only for the spectra converging toward the real axis at the low frequency part. The character of the DRT spectra is analogous to a high-entropy CAM spinel from our previous study[29], which appears to be a typical character for CAMs. Hence, the observed peaks can be assigned in a similar manner.[29–31] The high-frequency peak (ca. 10^5 Hz), not varying significantly during cycling, is labeled as $P_{contact}$ and corresponds to the contact impedance. The two intermediate-frequency peaks (ca. 10^3-10^5 Hz), labeled as P_{SEI}, are assigned to the polarization related to the SEI layer and charge transfer in the Li counter electrode (higher frequency peak, less variable with the lithiation level), and to the polarization effects from the SEI layer formed on the investigated electrode (peak centered at ca. 5·10^3 Hz). Similarly as for the high-entropy CAM, the SEI resistance related to the Zn_2SnO_4-based electrode decreases in the 1st cycle, as the film gets stabilized. It remains rather stable during the 2nd lithiation, except for the last point (full lithiation) where the SEI resistance noticeably increases. It can be interpreted as SEI cracking

during deep lithiation due to big volume changes, with a new, thicker film formation at the fresh surfaces exposed to the electrolyte. The peaks located in the range between 1 and 10^3 Hz, with a couple of maxima (the number depends on the lithiation level), are assigned to the polarization connected with charge transfer (P_{CT}) phenomena in the studied electrode. During the 1st lithiation, the properties of the pristine Zn_2SnO_4 change significantly, which is in line with the observed in operando XRD decomposition of the initial spinel structure (points 1-2). Then, upon further conversion and alloying processes, the charge transfer (CT) resistance continuously decreases. In the 1st delithiation and 2nd lithiation, two distinct regions related to the CT polarization can be named, with the clearly visible separation points between 12-14 and 18-20. This confirms the conversion-alloying character of the electrode, with the regions characterized by a higher resistance corresponding to the regime of the voltage profiles assigned to the conversion reaction (worse transport properties of oxide phase compared to metallic counterparts). The separation point between conversion and alloying is in agreement with the phase analysis based on operando XRD. It is worth noting that the resistance increase during 1st delithiation when moving to the conversion regime is much more pronounced than for the previously studied high-entropy spinel[29], which can be correlated with the unfavorable high polarization related to the Li_6ZnO_4/Li_4ZnO_3 phases formation.

Particular attention should be drawn to the differences in charge transfer (P_{CT}) at the points on the voltage profiles related to the proposed in this work formation of α-Sn and β-Sn (point 12, 1st delithiation, and point 24, 2nd lithiation, respectively, according to the phase composition study by operando XRD, Figure 2a-d), with the EIS data and corresponding DRT presented in Figure S2h-i. First of all, during the 1st delithiation, when the Sn phase starts to emerge (points 9-11), the CT resistance decreases. Therefore, even if the semiconducting α-Sn is formed[32,33], it is not a predominant factor influencing CT in this case. On the other hand, when the DRT spectra are directly compared for different Sn allotropes (according to operando XRD, while the remaining phases are similar between these two points), the total resistance in the whole frequency range is lower for the 2nd lithiation (including SEI and possible electronic transfer processes occurring at higher frequencies than P_{CT}). As α-Sn is semiconducting and β-Sn has a metallic character, this indirectly supports the claim about the formation of two different polymorphs of Sn in the 1st and 2nd discharge/charge cycles.

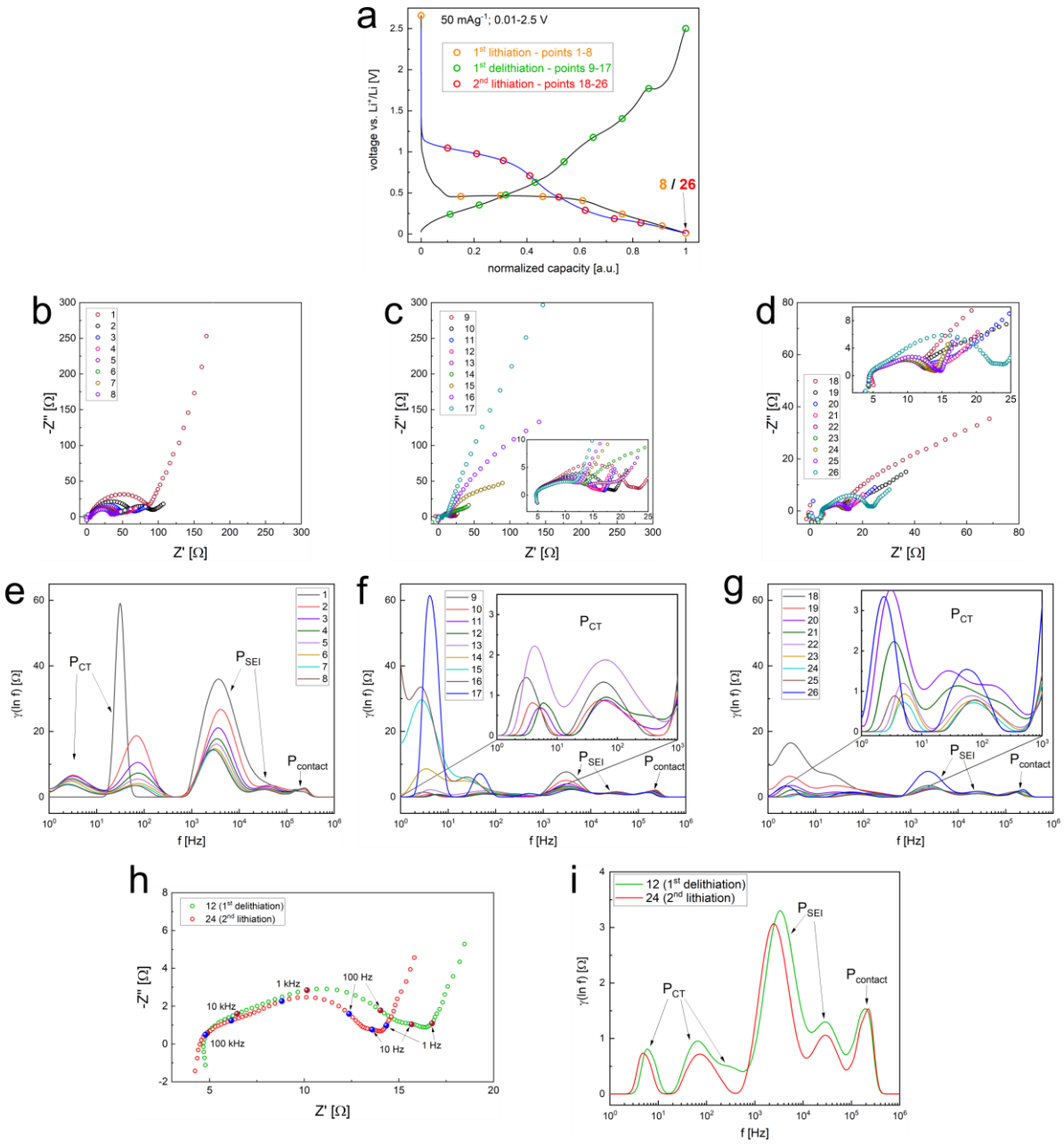

Figure S2. Charge transfer study at different (de-)lithiation stages for the Zn_2SnO_4 anode (CMC/SBR binder and $LiPF_6$ in EC:DEC electrolyte). (a) Normalized capacity voltage profiles for the 1st lithiation, 1st delithiation, and 2nd lithiation in the voltage range of 0.01-2.5 V under a specific current of 50 mA g^{-1}. The marked points correspond to the stages when EIS measurements were conducted; points 8 and 26 are overlapped. (b-d) EIS spectra measured at the marked points during the 1st lithiation (b), 1st delithiation (c), and 2nd lithiation (d) with the insets showing zoomed regions for clarity. (e-g) Distribution function of relaxation times as a function of frequency for the 1st lithiation (e), 1st delithiation (f), and 2nd lithiation (g) with the insets showing zoomed region corresponding to peaks assigned to the charge transfer polarization; $P_{contact}$ - peaks from the contact impedance; P_{SEI} - peaks related to the polarization from SEI layer and Li electrode; P_{CT} - peaks from the electrode's charge transfer polarization. (h-i) Selected EIS spectra measured at points corresponding to the formation of α-Sn (point 12) and β-Sn (point 24), according to the operando XRD study (h) with the corresponding DRT (i).

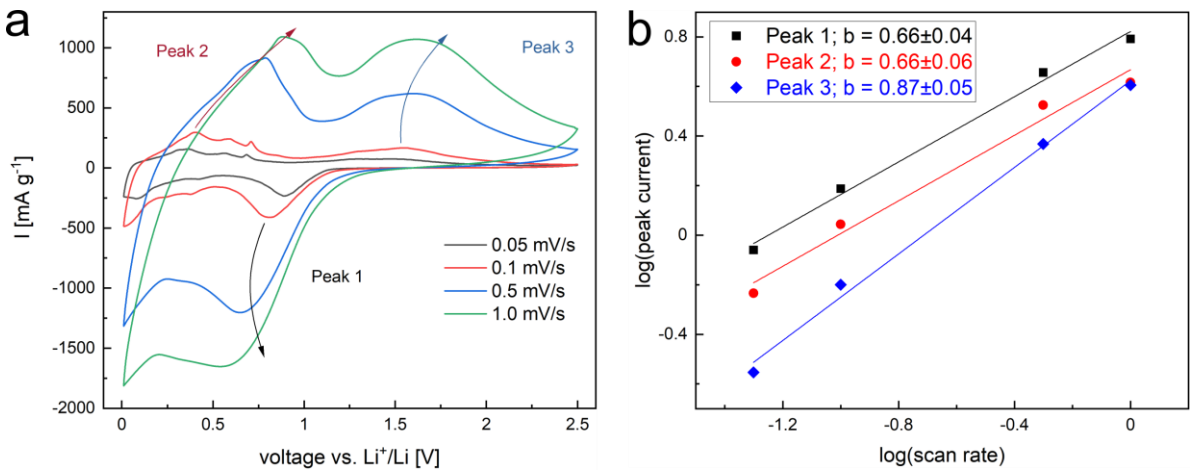

Figure S3. Analysis of the pseudo-capacitive influence on the Li-storage for the Zn_2SnO_4-based anode. (a) CV collected in the 0.01-2.5 V range with 3 cycles for each scan rate: 0.05, 0.1, 0.5, 1.0 mV s^{-1}. For clarity, the 2nd cycle for each scan rate is presented. The peaks taken for the analysis are marked. (b) Log(peak current) - log (scan rate) plot used to determine b-values according to the relationship between the scan rate and peak current $i = av^b$ (i - peak current; v - scan rate; a, b - parameters from a linear fitting of log-log plot)[34,35]. The b-value equal to 0.5 indicates the diffusion controlled storage, while b equal to 1 indicates the pseudo-capacitive controlled storage. The values obtained for the analyzed peaks indicate mixed, hybrid pseudo-capacitive and diffusion storage, where the alloying reaction is shifted more toward diffusion domination and the conversion reaction more toward pseudo-capacitive domination.

Table S2. Phases assigned in the SAED pattern with the measured and expected d-spacings for different phases. The differences between measured and expected values are below 4.3%, which lies within the experimental errors, especially considering the nanoscale dimensions of the crystallites in the sample.[33] The following phases were assigned: LZO = Li_6ZnO_4 (PDF 00-040-0202) / Li_4ZnO_3; LiZn (PDF 04-003-6868); β-Sn (PDF 00-004-0673); Li_2O (PDF 00-012-0254); Zn (PDF 00-004-0831).

Phase	Plane	Measured d-spacing [nm]	Expected d-spacing [nm]	Difference [%]
LiZn	(111)	0.350	0.359	2.7
β-Sn	(200)	0.291	0.292	0.4
β-Sn /LZO/Li_2O	(101)/(201)/(111)	0.276	0.279/0.267/0.266	1.1/3.2/3.6
Li_2O	(200)	0.236	0.231	2.2
Zn/β-Sn	(101)/(220)	0.205	0.209/0.206	1.9/0.4
β-Sn/LZO	(211)/(301)	0.199	0.202/0.197	1.6/0.9
LiZn	(311)	0.183	0.187	2.3
Zn/LZO/Li_2O	(102)/(222)/(220)	0.164	0.169/0.164/0.163	3.0/0.0/0.7
β-Sn	(112)	0.147	0.148	0.8
Li_2O/Zn	(311)/(103)	0.140	0.139/0.134	0.7/4.3

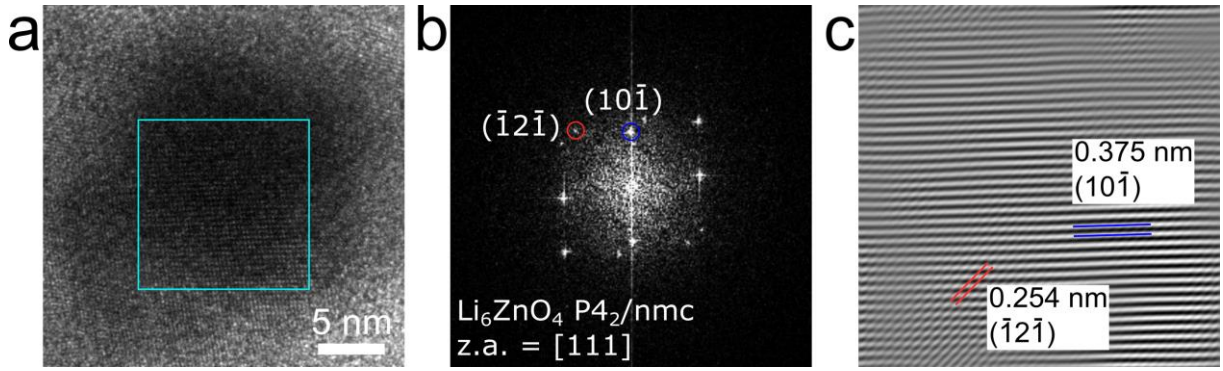

Figure S4. Selected nanoparticle showing a crystallite of the Li_6ZnO_4 phase. The sample corresponds to the XRD pattern at x = 36 % (0.52 V) in Figure 2c. (a) HR-TEM image with the FTT (b) with the selected peaks indexed as the tetragonal Li_6ZnO_4 phase. The remaining spots correspond to β-Sn phase (as visible in Figure 3d) and are not indexed here for clarity. (c) Inverse FTT for the selected spots marked with circles in (b).

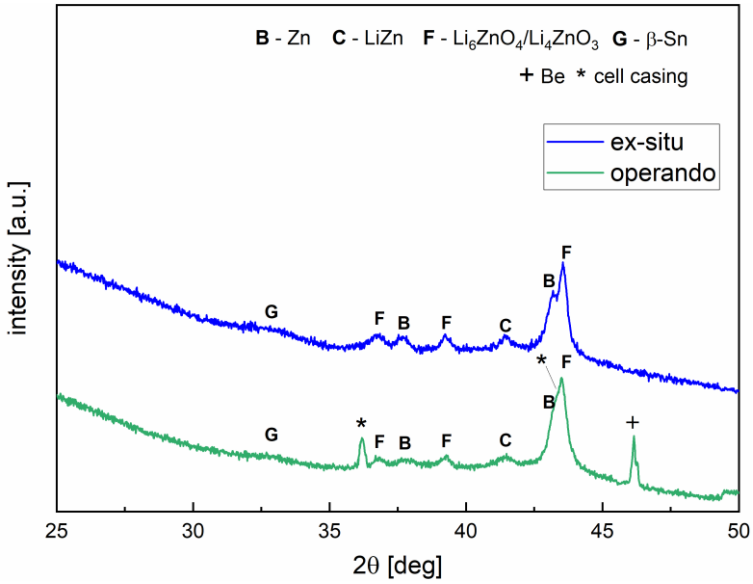

Figure S5. Comparison of the XRD pattern for the electrodes measured in the ex-situ and operando modes. The XRD pattern for the operando electrode corresponds to Figure 2c, x = 36%; 0.52 V. The patterns are in very good agreement, except for the Be-related and cell-casing-related additional peaks for the operando measurement. For the ex-situ sample all the phases could be assigned in the same way.

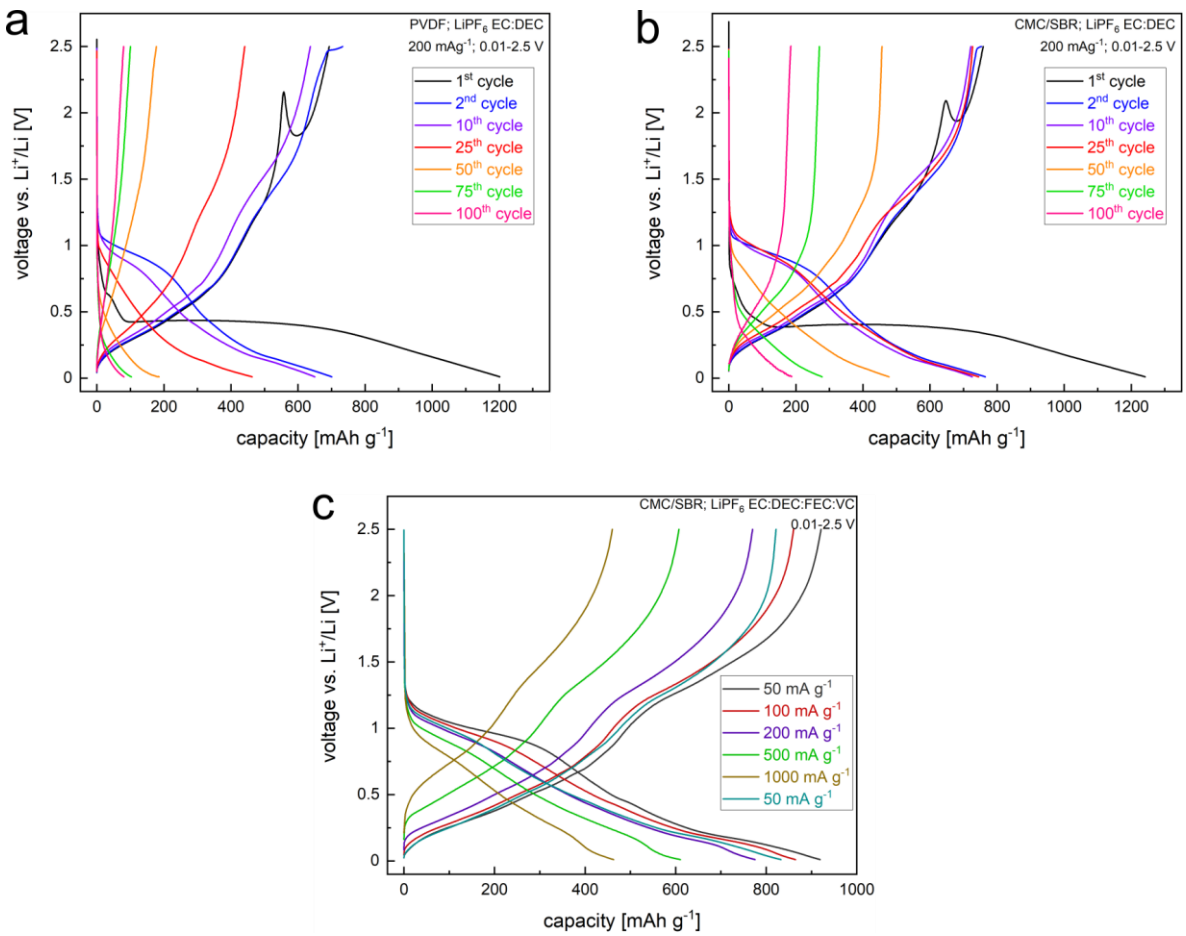

Figure S6. GDC curves for Zn_2SnO_4 half-cells tested with different binder/electrolyte setups. (a,b) Data corresponding to the long-term stability for 100 cycles presented in Figure 4b. (c) Data corresponding to the rate capability tests from Figure 4c for the best performing cell with CMC/SBR binder and $LiPF_6$ in EC:DEC:FEC:VC electrolyte.

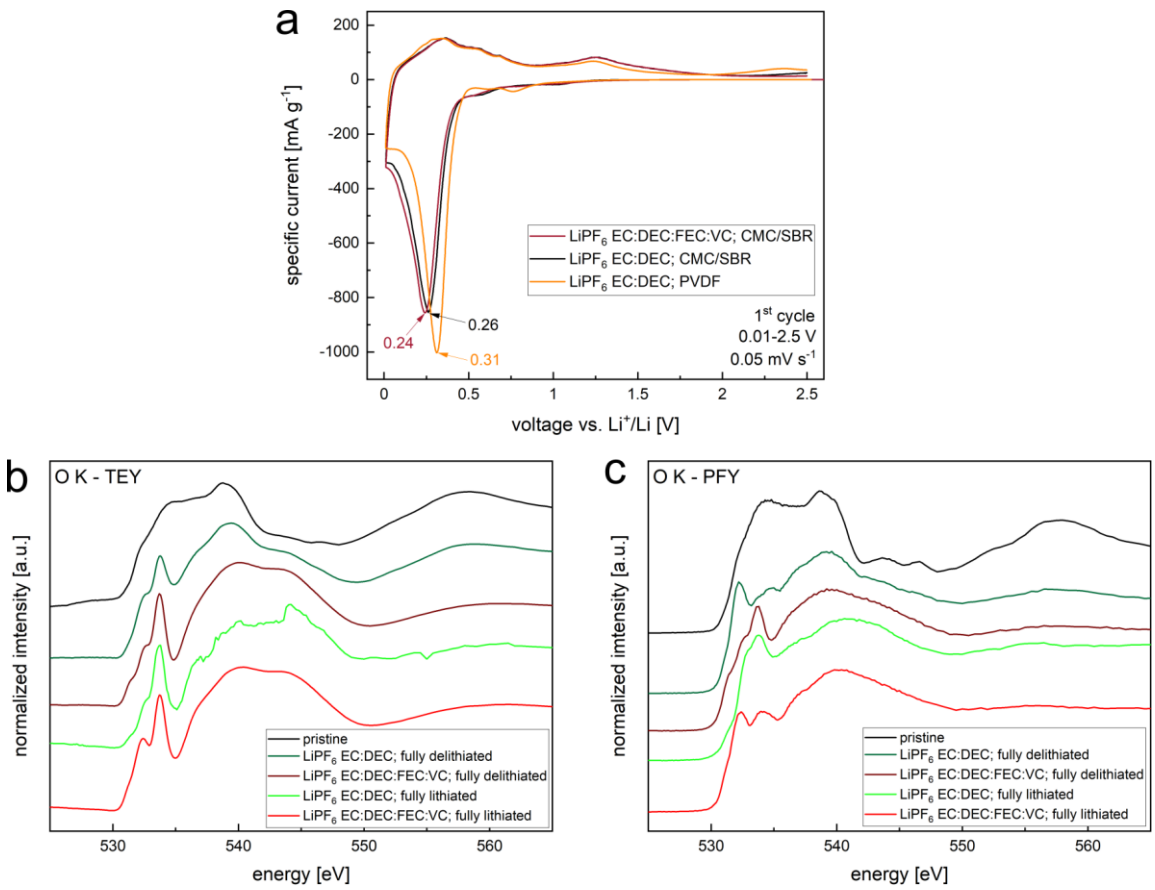

Figure S7. SEI formation studies. (a) Comparison of the 1st cycle cyclic voltammetry curves for Zn_2SnO_4 electrode with CMC/SBR and PVDF binders and with different electrolytes: 1M $LiPF_6$ in EC:DEC and 1M $LiPF_6$ EC:DEC:FEC:VC. (b,c) Ex-situ XAS studies of O K-edge for Zn_2SnO_4 anode with CMC/SBR binder in half-cells with different electrolytes: (a) measured in TEY mode (surface information) and (b) measured in PFY mode (bulk information, up to ca. 100 nm).

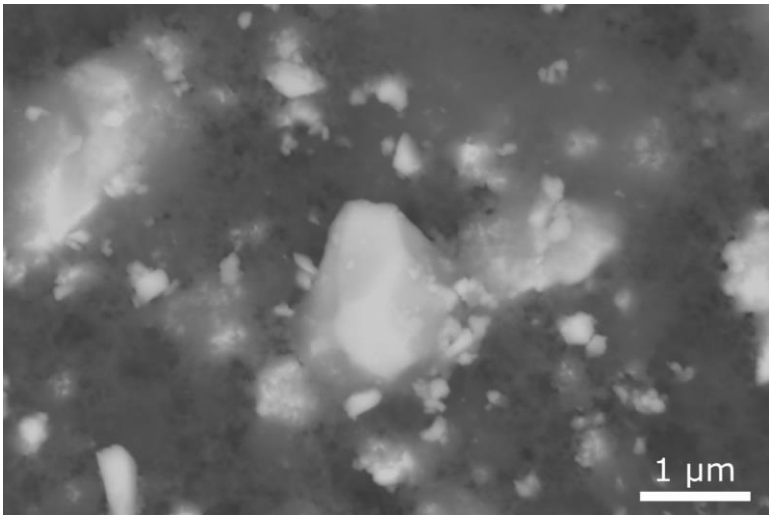

Figure S8. High magnification SEM image for the pristine electrode with CMC/SBR binder in BSE mode. The pristine particles are not agglomerated but distributed within carbon-binder matrix (the particle size is significantly higher than for the agglomerated nanoparticles visible in Figure 4e).

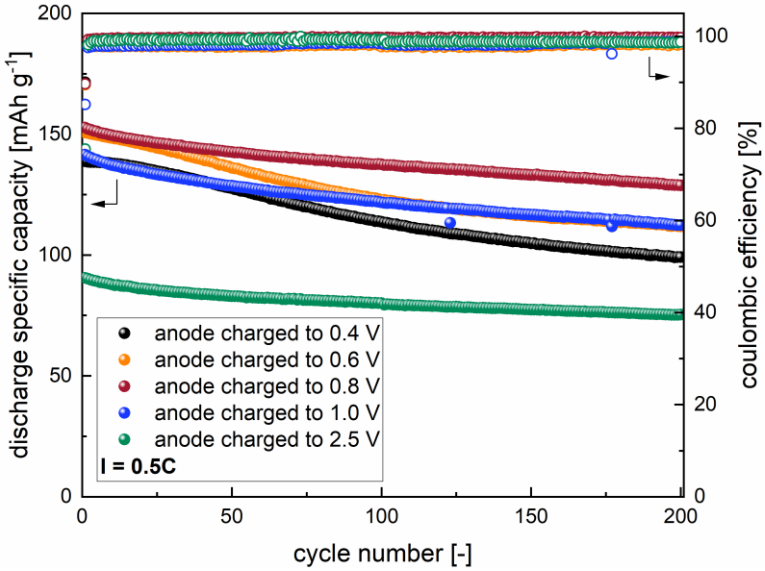

Figure S9. Long-term stability tests for the full-cells with anodes prelithiated to different voltages in the 2.25-4.2 V range under the current of 0.5C for 200 cycles.

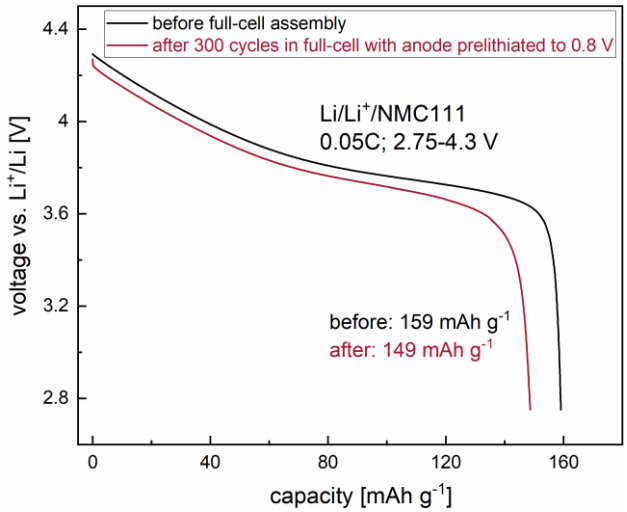

Figure S10. Assessment of the performance degradation in the full-cell from the cathode. The full-cell with the anode prelithiated to 0.8 V was disassembled after 300 cycles, used to make a fresh half-cell, charged to 4.3 V and discharged to 2.75 V under a current of 0.05C.

Table S3. Full-cell performance comparison with different electrode materials.

Cathode	Anode	Capacity* (mAh/g)	Energy density (Wh/kg)	Ref.
$LiCoO_2$	Fe_2O_3	800[a] (100 cycles)	123	[36]
$LiFePO_4$	$ZnMn_2O_4$	132[c] (100 cycles)	231	[37]
NCM111	TM-HEO	256[a] (100 cycles)	236	[38]
$LiNi_{0.5}Mn_{1.5}O_4$	$Co_{0.5}Zn_{0.5}Fe_2O_4$	100[c] (20 cycles)	350.8	[39]
Li-rich	$Mn_{0.8}Co_{0.2}O$	200[c] (20 cycles)	360	[40]
NCM111	**Zn_2SnO_4**	**120[c] (300 cycles)**	**367**	**this work**

*The capacity based on anode mass was marked "a", the capacity based on cathode mass was marked "c". TM-HEO: transition metal-based high-entropy oxide

References

1 N. Kim, J. Shim, W. Jae, J. Song and J. Kim, *J. Alloys Compd.*, 2019, **786**, 346–355.

2 L. Qin, S. Liang, X. Tan and A. Pan, *J. Alloys Compd.*, 2017, **692**, 124–130.

3 B. Wang, H. Wang, Y. Ma, X. Zhao, W. Qi and Q. Jiang, *J. Power Sources*, 2015, **281**, 341–349.

4 Y. J. Hong and Y. C. Kang, *Nanoscale*, 2014, **7**, 701–707.

5 L. Qin, S. Liang, A. Pan and X. Tan, *Mater. Lett.*, 2016, **164**, 44–47.

6 S. Yuvaraj, J. Lee and W. Lee, *RSC Adv.*, 2015, **5**, 67210–67219.

7 T. Jiang, X. Tian, H. Gu, H. Zhu and Y. Zhou, *J. Alloys Compd.*, 2015, **639**, 239–243.

8 X. Ji, X. Huang, Q. Zhao, A. Wang and X. Liu, *J. Nanomater.*, 2014, **2014**, 6.

9 Y. Zhao, Y. Huang, Q. Wang, K. Wang, M. Zong, L. Wang, W. Zhang and X. Sun, *RSC Adv.*, 2013, **3**, 14480–14485.

10 R. Zhang, Y. He and L. Xu, *J. Mater. Chem. A*, 2014, **2**, 17979–17985.

11 H. Fan, Z. Liu, J. Yang, C. Wei, J. Zhang and W. Zheng, *RSC Adv.*, 2014, **4**, 49806–49810.

12 W. Song, J. Xie, W. Hu, S. Liu, G. Cao, T. Zhu and X. Zhao, *J. Power Sources*, 2013, **229**, 6–11.

13 C. T. Cherian, M. Zheng, M. V. Reddy, B. V. R. Chowdari and C. H. Sow, *ACS Appl. Mater. Interfaces*, 2013, **5**, 6054–6060.

14 N. Feng, S. Peng, X. Sun, L. Qiao, X. Li, P. Wang, D. Hu and D. He, *Mater. Lett.*, 2012, **76**, 66–68.

15 X. Zheng, Y. Li, Y. Xu, Z. Hong, M. Wei, *CrystEngComm*, 2012, **6**, 2112–2116.

16 W. Song, J. Xie, S. Liu, G. Cao, T. Zhu and X. Zhao, *J. Mater. Res.*, 2012, **27**, 3096–3102.

17 W.S. Yuan, Y.W. Tian, L.J. Liu and J.Z. Li, *T. Nonferr. Metal. Soc.*, 2012, **22**, 858–864.

18 S. M. Becker, M. Scheuermann, V. Sepelák, A. Eichhöfer, D. Chen, R. Mönig, A. S. Ulrich, H. Hahn and S. Indris, *Phys. Chem. Chem. Phys.*, 2011, **13**, 19624–19631.

19 X. Hou, Q. Cheng, Y. Bai and W. F. Zhang, *Solid State Ionics*, 2010, **181**, 631–634.

20 W. S. Yuan, Y. W. Tian and G. Q. Liu, *J. Alloys Compd.*, 2010, **506**, 683–687.

21 J. Lee and C. Lee, *J. Supercrit Fluids*, 2010, **55**, 252–258.

22 X. J. Zhu, L. M. Geng, F. Q. Zhang, Y. X. Liu and L. B. Cheng, *J. Power Sources*, 2009, **189**, 828–831.

23 A. Rong, X. P. Gao, G. R. Li, T. Y. Yan, H. Y. Zhu, J. Q. Qu and D. Y. Song, *J. Phys. Chem. B*, 2006, **281**, 14754–14760.

24 J. Song, X. Lu, Q. Tian, L. Cui, J. Chen, Z. Sui, *J. Alloys Compd.*, 2022, **910**, 164924.

25 Y. R. Lim, C. S. Jung, H. S. Im, K. Park, J. Park, W. Il Cho and E. H. Cha, *J. Mater. Chem. A Mater. energy Sustain.*, 2016, **4**, 10691–10699.

26 C. Chen, Q. Ru, S. Hu, B. An and X. Song, *Electrochim. Acta*, 2015, **c**, 203–213.

27 H. Tang, C. Cheng, G. Yu, H. Liu and W. Chen, *Mater. Chem. Phys.*, 2015, **159**, 167–172.

28 S. Lei, K. Tang, C. Chen, Y. Jin and L. Zhou, *Mater. Res. Bull.*, 2009, **44**, 393–397.

29 M. Moździerz, K. Świerczek, J. Dąbrowa, M. Gajewska, A. Hanc, Z. Feng, J. Cieślak, M. Kądziołka-Gaweł, J. Płotek, M. Marzec and A. Kulka, *ACS Appl. Mater. Interfaces*, 2022, **14**, 42057–42070.

30 X. Chen, L. Li, M. Liu, T. Huang and A. Yu, *J. Power Sources*, 2021, **496**, 229867.

31 K. Pan, F. Zou, M. Canova, Y. Zhu and J. H. Kim, *J. Power Sources*, 2020, **479**, 229083.

32 N. Oehl, L. Hardenberg, M. Knipper, J. Kolny-Olesiak, J. Parisi and T. Plaggenborg, *CrystEngComm*, 2015, **17**, 3695–3700.

33 A. U. Haq, S. Askari, A. McLister, S. Rawlinson, J. Davis, S. Chakrabarti, V. Svrcek, P. Maguire, P. Papakonstantinou and D. Mariotti, *Nat. Commun.*, 2019, **10**, 1–8.

34 D. Wang, S. Jiang, C. Duan, J. Mao, Y. Dong, K. Dong, Z. Wang, S. Luo, Y. Liu and X. Qi, *J. Alloys Compd.*, 2020, **844**, 156158.

35 T. He, X. Kang, F. Wang, J. Zhang, T. Zhang and F. Ran, *Mater. Sci. Eng. R Reports*, 2023, **154**, 100737.

36 P. S. Veluri and S. Mitra, *ChemElectroChem*, 2017, **400076**, 686–691.

37 P. Xiong, L. Peng, D. Chen, Y. Zhao, X. Wang and G. Yu, *Nano Energy*, 2015, 816–823.

38 Q. Wang, A. Sarkar, Z. Li, Y. Lu and L. Velasco, *Electrochem. commun.*, 2019, **100**, 121–125.

39 M. L. López, C. Pico and M. L. Veiga, *Nano-Struct.*, 2017, **11**, 88–93.

40 B. Zou, Q. Hu, D. Qu, R. Yu, Y. Zhou and Z. Tang, *J. Mater. Chem. A*, 2016, **4**, 4117–4124.